



ELSEVIER

Physica D 105 (1997) 285–306

PHYSICA D

## Pattern formation in B-cell immune networks: Domains and dots in shape-space

A.J. Noest\*, K. Takumi, R. de Boer

*Department of Theoretical Biology, Utrecht University, Padualaan 8, NL-3584-CH Utrecht, Netherlands*

Received 6 May 1996; revised 30 October 1996; accepted 5 November 1996

Communicated by M. Mimura

---

### Abstract

The immune system contains many types of B-cells, which can activate each other if the shapes and surface properties of their receptors (or antibodies) match well. The dynamics of the resulting network is analysed using a recently derived B-cell activation function which captures the effects of the binding and crosslinking of B-cell receptors. All receptor/antibody shapes are parametrised by a continuous 'shape-space', such that matching pairs of shapes interact locally.

The model produces a variety of activation patterns across shape-space for a wide range of parameters. The spatio-temporal structures differ qualitatively from those seen with a previously used type of activation function. In either case, the pattern formation can largely be understood analytically, by first solving exactly for the various uniform fixed solutions, and then computing the evolution of spatially modulated perturbations. For the more realistic activation function, the following scenario is found.

Most (random) initial conditions first lead to the formation of coarse domains, of three possible types: the 'virgin'-(V) state, the 'immune/suppressed' (I/S)-state, and its reverse (S/I). V-domains are stable, but the other two types are unstable to spatial perturbations with a wavelength which is of the order of the interaction range. In the second stage, this instability causes big I/S- and S/I-domains to split up into arrays of small 'dots' which preserve the I/S-asymmetry of their parent domain. These dots are stable, even in isolation, which allows them to act as a 'memory' for previously encountered antigens.

No stable dots are obtained when the model is made to emulate the simpler activation function which has been used widely in earlier models. With this less realistic choice, unstable waves propagate from the boundaries of coarse I/S-domains, eventually filling up most of shape-space. This instability was previously described as 'percolation'.

*Keywords:* Pattern-formation; Immune network; Idiotypic network; B-cells; Modulation instability; Domains

---

### 1. Introduction

The immune system (see e.g. [1] for a non-specialist overview) provides an efficient (although not foolproof) protection against a bewildering variety of potentially lethal infective agents, many of which even change their characteristics through rapid evolution within a host. The immune system employs many types of cells, and most of

---

\* Corresponding author. Tel.: +31-30-2533695; fax: +31-30-2513655; e-mail: ajn@binf.biol.ruu.nl.

these function in an interdependent manner. To reduce this complexity to a tractable model, we explicitly represent just one of the cell types, namely the B-cells. These cells are capable of antigen recognition as well as antibody production, but only if there is sufficient help from T-cells. Here, we simply assume that this is the case.

Each B-cell carries one (quasi-random) type of receptor on its surface, and the shape (plus surface properties) of its receptor may match some part of the surface of an antigen (this part is called the ‘epitope’). This event activates the production of more copies of the B-cell in question, yielding a B-cell ‘clone’. Some of these cells will mass-produce and release their receptors in the form of antibodies. The antibodies bind to the matching epitope of the antigenic agents, marking them for destruction.

The variety of available B-cell receptors appears to be so great that almost any antigen will activate at least one B-clone. However, this extensive coverage implies also that a newly produced antibody should in turn activate some other B-cell clones which happen to match its shape sufficiently well; this forms an ‘idiotypic’ interaction [2]. In short, the set of B-cell clones becomes a network. The basic reason why the activity of even a single pair of matching clones does not blow up is that the cell activation function has a suppressive regime at high levels of stimulation, as explained later. This still leaves one with the task of understanding the dynamics of the network as a whole.

Functionally relevant aspects of the immune response, especially its possible long-term (memory) behaviour, may be expected to depend on collective effects of the B-cell network. The fact that the number of participating clones may be of the order  $10^6$  makes the analysis of such effects difficult in general, but the problem can be made much more tractable by the introduction of a (relatively low-dimensional) ‘shape-space’, which parametrises the receptor surface characteristics and relates the idiotypic interaction to a notion of shape-distance [3,4]. Collective effects can then be studied in terms of the structure and dynamics of clonal activity patterns on shape-space.

Network stability studies using widely accepted (single-field) clone activation models have found that perturbations of a single clone tend to propagate through the system, both in a discrete-clone (e.g. [5]) and in a shape-space (e.g. [4]) setting. This appears to be an unrealistic prediction. However, recent work [6,7] using a more realistic two-field clone activation [8] indicates the emergence of more stable and localised response modes. These and many related differences in functionally important network behaviour are explained by our analysis and simulations, which focus on the formation of spatio-temporal patterns of clonal activity across shape-space. Our model includes earlier models as special cases, allowing us to explain the origins of the different behaviours.

The general approach is as follows: First, we construct the uniform fixed-point solutions, and sketch the flow field which governs the evolution of uniform states. Next, we analyse (in)stabilities with respect to spatial modulations. This yields several predictions about multi-stage spatial pattern formation, which we then compare to numerical simulation results. Most of the phenomenology is described well by the analytical results, despite the fact that the pattern formation is often controlled by two or three different instabilities acting sequentially or concurrently before the system settles into a stable pattern.

## 2. Model construction

### 2.1. Dynamics of individual clones

The number of cells  $b_i$  of a clone  $i$  evolves according to

$$\partial_t b_i = s + b_i \left[ \frac{p\theta}{\theta + b_i} f(h_i, h'_i) - d \right], \quad (1)$$

where  $s$  is the (small) rate of influx,  $p$  the maximal growth rate,  $\theta$  the (large) clone-size at which further growth is assumed to decrease,  $d$  the death rate, and  $f(h_i, h'_i)$  is the normalised cell activation function,

$$f(h_i, h'_i) = \frac{(1 + 4w)h'_i}{w(1 + h_i)^2 + h'_i}, \tag{2}$$

as derived [6,8] from the chemistry of equilibrium receptor binding and crosslinking. Typical parameter values are  $w = \frac{1}{10}$ ,  $p = 2$ ,  $\theta = 100$ ,  $d = 1$ , and  $s = 10^{-4}$ .

The binding field  $h_i$  is defined as

$$h_i = \sum_j K_{ij} b_j, \tag{3}$$

and the crosslinking field  $h'_i$  as

$$h'_i = \sum_j K_{ij}^{\eta+1} b_j, \tag{4}$$

where  $\eta$  parametrises the relation of the two steps (binding and crosslinking) required for cell activation. The choice  $\eta = 1$  models the plausible situation in which the crosslinking rates are proportional to the binding rates [6,8]. Earlier models (e.g. [4,5]) neglected the correlation between the two steps; the essence of this situation can be

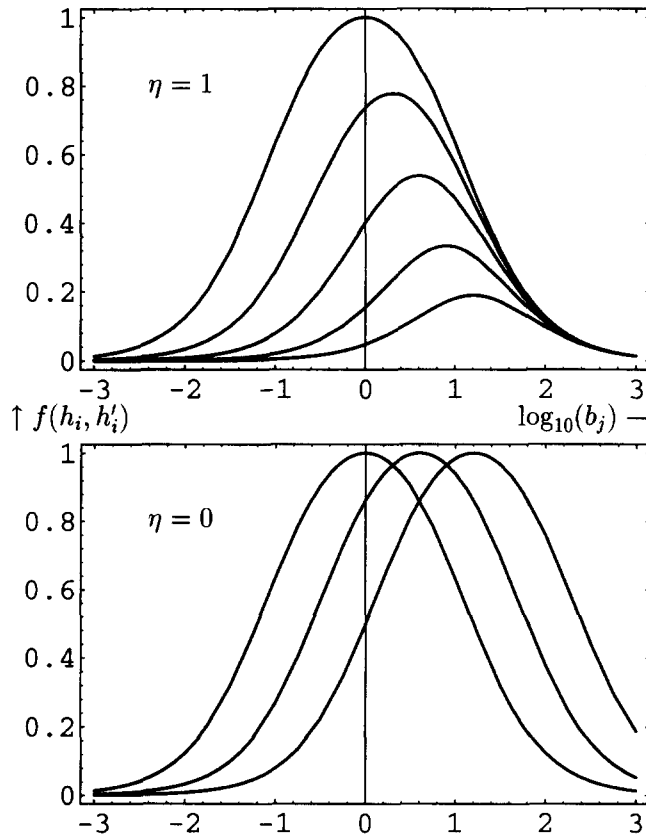


Fig. 1. Activation function  $f(h_i, h'_i)$  for a clone  $i$  activated by a single other clone  $j$ , i.e. with  $h_i = K b_j$  and  $h'_i = K^{\eta+1} b_j$ . The top panel (with  $\eta = 1$ ) shows the function for  $K = 1, \frac{1}{2}, \frac{1}{4}, \frac{1}{8}, \frac{1}{16}$ ; the function decreases with  $K$  at any  $b_j$ , producing a nested family of graphs. In the bottom panel, with  $K = 1, \frac{1}{4}, \frac{1}{16}$ , the graphs only shift rightwards. The maxima occur at  $b_j = 1/K$ , for any  $\eta$ . See [8] for the derivation of  $f(h_i, h'_i)$ .

modelled by setting  $\eta = 0$ . For either choice of  $\eta$ , the overall activation  $f(h_i, h'_i)$  of a clone is bell-shaped when plotted against the  $\log(b_j)$  level of a single other clone; see any of the plots in Fig. 1. Note that survival of clone  $i$  requires  $f(h_i, h'_i) > d/p$ ; otherwise, it is essentially sustained by the small influx  $s$  only. With  $\eta = 1$ , the  $b_j$ -interval for which clone  $i$  survives, shrinks with decreasing  $K$  and eventually disappears; see Fig. 1, upper panel. In the older models ( $\eta = 0$ ), the survival interval merely shifts to higher values of  $b_j$ ; see Fig. 1, lower panel.

In the first paper which employed the two-field activation function in immune network modelling [6], a somewhat simpler clone-dynamics was used, namely

$$\partial_t b_i = s + b_i[pf(h_i, h'_i) - d]. \quad (5)$$

This is formally the limiting case  $\theta \rightarrow \infty$  of Eq. (1), so the simplification corresponds to a lack of clonal self-limitation. The qualitative behaviour of these equations is often similar, but the presence of self-limitation prevents some non-generic (and probably unrealistic) behaviour for small  $s$ .

## 2.2. Shape-space and interaction structure

Given some set of clones  $i$  and their couplings  $K_{ij}$ , the evolution of the  $b_i$  can be computed – in principle – from Eqs. (1)–(4), but analysing the behaviour of the system becomes difficult in general as soon as there are more than two or three significantly interacting clones. In fact, the variety of interacting B-cell clones is (potentially) many orders of magnitude larger. One way of making analysis possible at this scale of the problem is to exploit the reasonable assumption that the  $K_{ij}$  are not independent, but reflect an underlying geometric structure of relatively low dimensionality, called a shape-space.

The rationale behind the use of such shape-spaces (introduced in [9]) is that  $K_{ij}$ -values probably depend on a limited set of parameters which describe the effective shape and physico-chemical properties of the B-cell receptor. In essence,  $K_{ij}$  should be large only when the (generalised) shapes of  $i$  and  $j$  ‘match’ well. Physically, this should imply that the geometry and charge distribution of the two epitopes are roughly each other’s inverse, while their distributions of e.g. hydrophobic or hydrogen-bridging sites should be similar. The usual formalisation of this is roughly as follows: The (smooth) parametrisation of generalised shapes is interpreted as a (metric) shape-space, so that each clone  $i$  corresponds to a distinct point  $x_i$  in shape-space. A map  $\mu$  (with  $\mu^2$  the identity) relates any shape  $x_i$  to its ideally matching shape  $x'_i$ . The coupling  $K_{ij}$  between clones  $i$  and  $j$  is then taken to be a decreasing function of the distance between  $x_i$  and  $x'_j$ , for example

$$K_{ij} = K \exp\left(-\frac{|x_i - x'_j|^2}{2\sigma^2}\right). \quad (6)$$

One has  $|x_i - x'_j| = |x'_i - x_j|$ , reflecting the fact that  $K_{ij}$  is  $i, j$ -symmetric since it is a chemical equilibrium constant. From an empirical point of view, one may consider the  $K_{ij}$  as given, and the shape-space as implicitly defined by the correlations among the  $K_{ij}$ . In principle, a realistic shape-space could be reconstructed from measured  $K_{ij}$ -values, on the assumption that Eq. (6), or some monotone transformation of it, fixes the metric.

In this paper, we simply assume a shape-space geometry which is convenient for our purposes: To simplify notation, we associate each *pair* of matching shapes with a single point  $x$  in the space, and take  $x \in \mathbb{R}^n$ . To distinguish between the two clones at each point  $x$ , we label their levels  $b_i(x)$  by indices  $i \in 1, 2$ . This replaces the original labelling  $i \in 1, \dots, N$  which disregards the continuity of shape-space. The assignment of the new

indices  $i \in \{1, 2\}$  is assumed to be globally continuous in  $x$ , which guarantees that only clones of unequal index can interact.<sup>1</sup> We no longer need the  $(x, x')$  notation for matching shapes, which will prove convenient.

To fit the continuous- $x$  setting, we rewrite the fields in terms of spatial convolutions,

$$h_i(x) = g \star b_j(x), \quad h'_i(x) = g^{\eta+1} \star b_j(x) \quad (7)$$

with  $\star$  denoting the  $n$ -dimensional convolution operator, e.g.  $g \star b(x) = \int d^n \xi g(\xi) b(x - \xi)$ . The kernels  $g(\xi) = K \exp(-\xi \cdot \xi / (2\sigma^2))$  and  $g^{\eta+1}(\xi)$  replace the original couplings  $K_{ij}$  and  $K_{ij}^{\eta+1}$  in the binding and crosslinking fields.

One may note that the crosslinking field kernel  $g^{\eta+1}(\xi)$  has a smaller effective width  $\sigma/\sqrt{\eta+1}$  than the width  $\sigma$  of the binding field kernel whenever  $\eta > 0$ . Combining this with the fact that  $\partial f(h_i, h'_i)/\partial h_i < 0$  while  $\partial f(h_i, h'_i)/\partial h'_i > 0$  suggests [6] that the system incorporates a form of ‘lateral inhibition’, which generally promotes the formation of spatially modulated or localised patterns. The body of this paper consists of a detailed investigation of this suggestion.

### 3. Analysis of shape-space pattern formation

As a concrete first example that will motivate much of the analysis which follows, Fig. 2 shows the formation of patterns in the clone levels across a one-dimensional shape-space (with periodic boundary conditions). The patterns were obtained by numerical integration of Eqs. (1)–(4) with the convolution-based fields (7). Except for small random perturbations, the initial conditions were uniform, and equal for  $i = 1, 2$ .

Even cursory inspection reveals two major stages in the pattern formation: First, the initial low-level (light-grey) state breaks up into irregular-sized domains, having either near-zero (white) or high (dark-grey) levels  $b_i(x)$ , but without breaking the  $i = 1, 2$  symmetry, thus far. The former domains remain stable, but the smaller high-level domains break up into (quasi-)regular arrays of ‘dots’. Each dot consists of a pair of co-localised peaks in the clone levels  $b_1(x), b_2(x)$ , with either  $b_1(x) > b_2(x)$  or  $b_1(x) < b_2(x)$  (the two dot types are related by exchanging  $i$  and  $j$ ). One also notices that the  $b_i(x)$  levels in dots show a damped temporal oscillation, which is in-phase between nearby dots of the same  $i = 1, 2$ -polarity. Within larger high-level domains, the break-up into dots is preceded by a coarser-scale break-up which determines the  $i = 1, 2$ -polarity of groups of neighbouring dots on a scale smaller than the original domain size.

A more precise characterisation of these patterns will emerge in the course of our analysis; for now, Fig. 2 merely exemplifies the ordering phenomena that we aim to explain. We will also address related patterns which form from other initial conditions, as well as different types of patterns which occur when our model is made to emulate previous immune network models.

As usual, the problem of analysing pattern formation from arbitrary initial conditions is difficult to solve in full generality, but a useful approach is to construct the uniform fixed-point solutions, and analyse their stability to perturbations of any wavelength. The most unstable wavelength then lays down a basic pattern which usually persists during the highly nonlinear later stages. In the present model, however, several instabilities at various scales can occur sequentially or concurrently before the solution approaches the final state.

<sup>1</sup> Strictly speaking, we should specify a fibre bundle structure to express the global topology implied by assigning the otherwise arbitrary labels  $i \in \{1, 2\}$ . In this paper, however, we only deal with a ‘trivial’ bundle structure, so there is no need for sophistication. Our choice excludes the existence of self-matching shapes and certain topological constraints on globally ordered patterns, even though such features could well occur in realistic shape spaces. The analysis of such cases is left until another occasion.

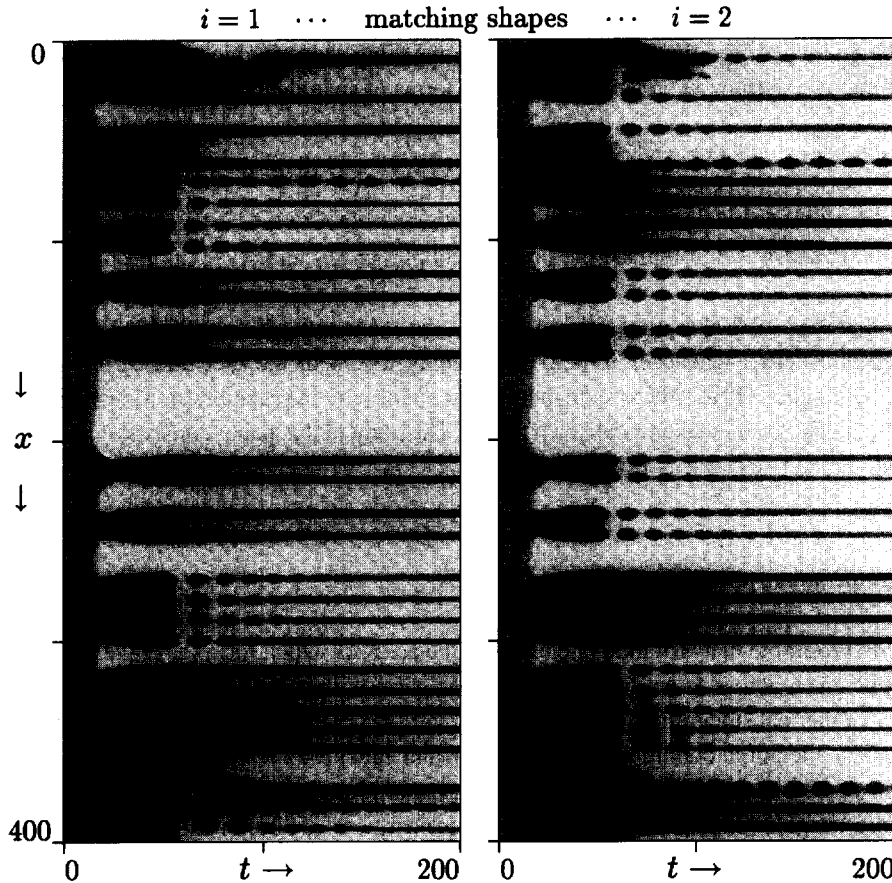


Fig. 2. Pattern formation in the two-field model ( $\eta = 1$ ), starting from a (weakly perturbed) uniform symmetric state ('L', see Section 3). The evolving clone levels  $b_i(x)$  are shown as grey-scale coded space-time  $(x, t)$  plots (white = 0, black = 100). The shape-space  $x$  is one-dimensional, with length 400 and circular boundary conditions. Other parameters are 'standard' (as in Table 1). See text for interpretation of pattern formation processes.

### 3.1. Uniform solutions

When considering only uniform solutions, we drop the  $x$ -dependence, and write  $b_i(x) = b_i$ ,  $h_i(x) = h_i$  and  $h'_i(x) = h'_i$ . Convolutions like  $g \star h(x)$  then trivialise to products, and it will prove useful to write  $h_i = \kappa b_j$  and  $h'_i = \gamma h_i$ . The new parameters

$$\kappa = K(2\pi)^{n/2}\sigma^n, \quad \gamma = K^\eta(\eta + 1)^{-n/2} \tag{8}$$

contain the integrals over the  $n$ -dimensional kernels  $g(x)$  and  $g^{n+1}(x)$ . The activation function  $f(h_i(x), h'_i(x))$  (Eq. (2)) degenerates into a function of one variable  $b_j$ , so we use the replacement

$$f(h_i, h'_i) \Rightarrow \phi(b_j) = \frac{(1 + 4w)\gamma\kappa b_j}{w(1 + \kappa b_j)^2 + \gamma\kappa b_j}. \tag{9}$$

The maximum of  $\phi(b_j)$  occurs at  $b_j = 1/\kappa$ , with value  $\phi(1/\kappa) = \gamma(1 + 4w)/(\gamma + 4w)$ . This maximum essentially controls the existence of the uniform fixed-point solutions, as explained below.

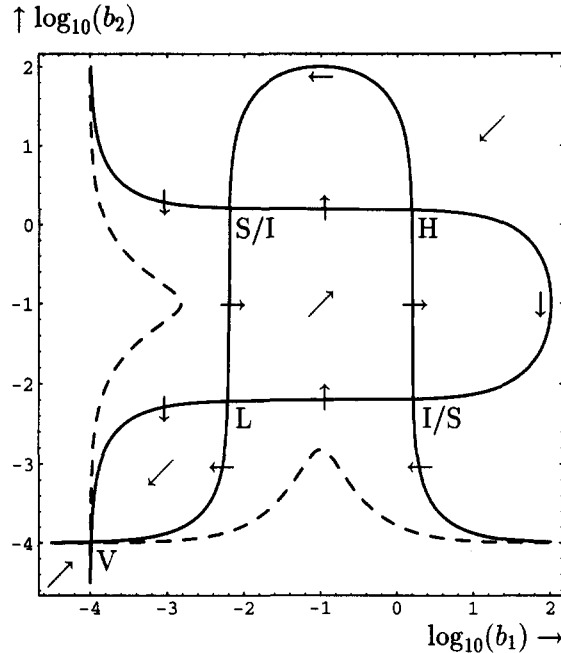


Fig. 3. Graphs of the  $(i = 1, 2)$ -pair of uniform fixed point equalities (null-clines). Solutions (graph intersections) are indicated by the letters V, L, H (on diagonal), and I/S or S/I; see text for terminology. Continuous-line graphs are for  $\gamma = 1, \kappa = 10$ , and  $s = 10^{-4}$ . Arrows indicate the flow-field direction on each section of the graphs, and on the diagonal. Dashed-line graphs are similar, except for  $\gamma = \frac{1}{5}$ ; this yields a case in which the V-state is the only uniform(!) solution.

3.1.1. Symmetric and asymmetric uniform fixed points

Uniform fixed-points are joint solutions of the pair of equalities  $\partial_i b_i = 0; i \in \{1, 2\}$ . Solutions of each of these equalities separately are the ‘null-clines’ of the  $(b_1, b_2)$ -flow. For general  $s$ , the fixed-point equalities can be rewritten as a pair of quadratic equations

$$-db_i^2 + [p\theta\phi(b_j) - d\theta + s]b_i + s\theta = 0. \tag{10}$$

It can be shown that only the larger root of each of these equations is relevant (positive) for any  $s > 0$ . In Appendix A, we sketch how all uniform fixed-point solutions can be found in exact closed form for arbitrary model parameters. The construction presents no substantial problems when using standard computer-algebra, but the resulting expressions are much too large to warrant being written down here. A more intuitively accessible, albeit qualitative, version of the construction is described here.

The uniform fixed points we seek can be represented by the intersections of the two graphs given by Eq. (A.1). Characteristic examples of the graphs and their intersections are shown in Fig. 3.

The possible shapes of the graphs and the nature of their intersections can be understood at least semi-quantitatively by focusing on the case  $s \rightarrow 0^+$  (with finite  $\theta$ ). This simplifies the fixed-point equalities to

$$b_i = \max \left[ \theta \left( \frac{p}{d} \phi(b_j) - 1 \right) \right]. \tag{11}$$

With  $s = 0$  precisely, the trivial  $b_i = 0$  solution exists for any value of  $\phi(b_j)$ , but it disappears for any  $s > 0$  over the interval where  $\phi(b_j) > d/p$ . This leaves us with Eq. (11) in the relevant limit  $s \rightarrow 0^+$ . Appendix A (see Eqs. (A.4) and (A.5)) shows how one may perturb Eq. (11) for realistically small  $s > 0$ .

The one-hump shape of  $\phi(b_j)$  will show up (partially) in the graphs of Eq. (11) as long as  $\max(\phi(b_j)) > d/p$ , i.e.  $\gamma(1+4w)p > d(\gamma+4w)$ . Depending on the height of the peak in each graph, there can be up to five fixed-point solutions. At most three of these are symmetric, i.e. on the diagonal  $b_1 = b_2$ . Clearly, if one of the graphs intersects the diagonal in some point, then the same must be true for the other graph, because the model is  $i, j$ -symmetric.

The symmetric ( $b_1 = b_2$ ) states are:

- The ‘virgin’ (V)-state. For  $s = 0$ , this is the trivial fixed point  $b_1 = b_2 = 0$ . For small  $s > 0$ , the V-state levels become  $b_1 = b_2 \approx s/d$ . At unrealistically large  $s$ , the V-state annihilates with the L-state (see below), but this is of no interest to us.
- The ‘low’ (L)- and ‘high’ (H)-symmetric states. For  $s = 0$ , the simple behaviour of Eq. (11) noted above gives rise to either no intersections with the diagonal (implying the absence of any solution besides V), or to two intersections, which we label ‘L’ and ‘H’ to reflect their lower or higher  $b_i$ -levels. We may neglect the non-generic case of tangency, where  $L = H$ . For realistically large  $\theta$ , the maximum of the graph crosses the diagonal very soon after it first shows up at all, i.e. for  $\gamma(1+4w)p > d(\gamma+4w)$ .

There may also be a pair of asymmetric ( $b_1 \neq b_2$ ) solutions:

- The ‘immune–suppressed’ states (I/S, and S/I). This pair of states bifurcates from an existing H-state when the derivative of Eq. (11) at H becomes less than  $-1$ . For realistically high values of  $\theta$ , this again happens very soon after the L- and H-states are born for increasing peak-height of Eq. (11). Under most conditions, the levels  $b_1, b_2$  in the I/S-states differ by a large amount. By convention, we name the state with  $b_1 > b_2$  the I/S-state, and vice versa. The terms ‘immune’ and ‘suppressed’ refer to the fact that in the I/S-state,  $\partial b_1 / \partial b_2 > 0$ . The ‘immune’ clone thus increases under additional stimulation, providing an immune response when a matching antigen arrives. A weak, inverse response occurs for the suppressed clone.

For realistically small  $s$ , the  $b_i$ -levels of the L-, H-, and both I/S-states, as well as the bifurcation points at which these states are born, only shift slightly without affecting their general character. The limiting case  $\theta \rightarrow \infty$  has similar uniform states (for  $s > 0$ ), although the way in which they bifurcate can differ. This will not be discussed further.

It is worth recalling that  $\gamma$  decreases exponentially with the dimension  $n$  (Eq. (8)) for any  $\eta > 0$ . The resulting decrease of  $\max(\phi(b_j))$  with  $n$  eventually destroys all uniform fixed points except the V-state. For moderate values of  $n$ , all five uniform fixed points could be maintained by allowing  $\kappa$  to grow sufficiently fast with  $n$ , but this cannot prevent  $\max(\phi(b_j))$  from falling below  $d/p$  eventually. For our standard parameters, this happens for  $n \geq 5$ . Most of the analysis below deals with the regime where all five states exist (but see the concluding remarks on the alternate regime).

### 3.2. Linear (in)stability to spatial modulations

In this section, we analyse the stability of each of the uniform fixed points to spatially modulated (and uniform) perturbations of the  $b_i(x)$ . The resulting predictions for pattern formation will be made explicit in Section 3.3, where we compare the theory with numerical simulations.

Each of the uniform fixed-point solutions  $b_i(x) = b_i$  can be perturbed to  $b_i(x) = b_i + \beta_i(x)$ . To first order, the Fourier components of  $\beta_i(x)$  evolve independently, so we need only consider individual components. Moreover, the translation invariance and isotropy of the shape-space allow us to choose the phase and wave vector direction of the component at will without losing generality. Thus, we use  $\beta_i(x) = \alpha_i \cos(kx)$ , where the spatial frequency  $k$  is the only new free parameter.

With this perturbation, the two fields become

$$h_i(x) = \kappa \left[ b_j + \exp\left(-\frac{\sigma^2 k^2}{2}\right) \alpha_j \cos(kx) \right], \tag{12}$$

$$h'_i(x) = \gamma \kappa \left[ b_j + \exp\left(-\frac{\sigma^2 k^2}{2(\eta + 1)}\right) \alpha_j \cos(kx) \right] \tag{13}$$

with the  $k$ -dependent exponentials coming from the Fourier transform of the convolution kernels. For  $\eta > 0$ , the field  $h'_i(x)$  has a larger spectral bandwidth than  $h(x)$ , corresponding to the smaller spatial width of  $g^{\eta+1}(x)$  relative to  $g(x)$ .

To first order in  $\alpha_i$ , the perturbed clone activation may be written as

$$f(h_i(x), h'_i(x)) = \phi(b_j) + c_i \alpha_j \cos(kx) \tag{14}$$

with

$$c_i = \kappa D_i \exp\left[-\frac{\sigma^2 k^2}{2}\right] + \gamma \kappa D'_i \exp\left[-\frac{\sigma^2 k^2}{2(\eta + 1)}\right], \tag{15}$$

where  $D_i$  is the value of the derivative  $\partial f(h_i, h'_i)/\partial h_i$  at the uniform fixed point  $h_i = \kappa b_j$ ,  $h'_i = \gamma \kappa b_j$ , and  $D'_i$  is the value of  $\partial f(h_i, h'_i)/\partial h'_i$  at the same fixed point. Explicitly, one has

$$D_i = -2 \frac{(1 + 4w)w\gamma\kappa b_j(1 + \kappa b_j)}{(w(1 + \kappa b_j)^2 + \gamma\kappa b_j)^2}, \tag{16}$$

$$D'_i = \frac{(1 + 4w)w(1 + \kappa b_j)^2}{(w(1 + \kappa b_j)^2 + \gamma\kappa b_j)^2}, \tag{17}$$

showing that  $D_i < 0$  and  $D'_i > 0$ . Thus, the perturbations in the binding and crosslinking fields oppose each other at the level of the activation functions  $f(h_i(x), h'_i(x))$ . Given the bandwidth differences between the two fields noted above, the  $k$ -dependence of the ‘gain’  $c_i$  in  $f(h_i(x), h'_i(x))$  can be non-monotonic when  $-D_i$  and  $\gamma D'_i$  are of the same order of magnitude. The graph of  $c_i$  versus  $k$  then shows a hump between the effective cut-off frequencies of the two fields. This feature can cause finite- $k$  instabilities, as will appear below.

After linearising the remaining terms containing  $b_i(x)$  ( $i \in 1, 2$ ), and collecting terms containing  $\beta_i(x)$ , we end up with a pair of ODEs for the cosine amplitudes  $\alpha_i$ , of the general form

$$\partial_t \begin{pmatrix} \alpha_1 \\ \alpha_2 \end{pmatrix} = \begin{pmatrix} A_{11} & A_{12} \\ A_{21} & A_{22} \end{pmatrix} \begin{pmatrix} \alpha_1 \\ \alpha_2 \end{pmatrix}. \tag{18}$$

The diagonal elements of the Jacobian matrix  $A$  are given by

$$A_{ii} = \frac{p\theta^2}{(\theta + b_i)^2} \phi(b_j) - d, \tag{19}$$

which is manifestly independent of  $k$ . Moreover, one finds  $A_{ii} < 0$  at any of the uniform fixed points  $(b_1, b_2)$ . The off-diagonal elements, on the other hand, are given by

$$A_{ij} = \frac{p\theta b_i}{\theta + b_i} \left\{ \kappa D_i \exp\left[-\frac{\sigma^2 k^2}{2}\right] + \gamma \kappa D'_i \exp\left[-\frac{\sigma^2 k^2}{2(\eta + 1)}\right] \right\}, \tag{20}$$

reflecting the  $k$ -dependence of the activation functions which we discussed earlier. One may note that the  $k$ -dependence of  $A$  has the opposite structure as the one found in the classical Turing analysis, where only the diagonal elements are  $k$ -dependent. Nevertheless, the determinant of  $A$  can still change sign as a function of  $k$ , leading to instabilities for finite  $k$  (or  $k = 0$ ).

As always, instability of a certain uniform fixed-point solution to perturbations with a wavelength  $L = 2\pi/k$  corresponds to a positive real part of a ( $k$ -dependent) eigenvalue of the Jacobian  $A$ . In fact, the linearised evolution of any small (and Fourier representable) perturbation  $\beta_i(x)$  can be computed and understood most easily in the Fourier domain, using the  $k$ -dependent eigenvalues and eigenvectors of  $A$ .

Using the closed forms for the uniform fixed points, the Jacobian and its eigensystem can be given exactly, but the results are of course too unwieldy to reproduce them here. Nevertheless, they can be used for computer-assisted determination of the stable and unstable regimes.

To illustrate the typical results obtained, we plot the real part of the dominant eigenvalue ( $\lambda_1$ ) of  $A$  as a function of  $k$ , computed at each of the uniform fixed points, and using a realistic choice of the other parameters (see Table 1). The same ‘standard’ parameters were used in computing the pattern (Fig. 2) shown earlier in the paper, and they will be used in all simulations to be shown below. Qualitatively similar behaviour occurs in a very wide range of parameters surrounding the ‘standard’ values.

Fig. 4 shows the real part of the dominant eigenvalue (denoted by  $\text{Re}(\lambda_1)$ ) as a function of  $k$ , for the asymmetric (I/S, or S/I) fixed point and for a few values of  $\eta$ . For any  $\eta$ , one finds the I/S-state to be stable to uniform (i.e.  $k = 0$ ) perturbations. At  $k = 0$ , the two eigenvalues have finite (opposite) imaginary parts, so the I/S-state would

Table 1  
Parameters used in all plots of  $b_i(x, t)$  and  $\lambda_1(k)$ , unless stated otherwise

‘Standard’ parameters	
Max. growth rate	$p = 2$
Death rate	$d = 1$
Self-limitation level	$\theta = 100$
Influx rate	$s = 10^{-4}$
$f(h, h')$ – width	$w = 0.1$
Max. binding constant	$K = 1$
Binding kernel width	$\sigma = 3$
Shape-space dimension	$n = 1$

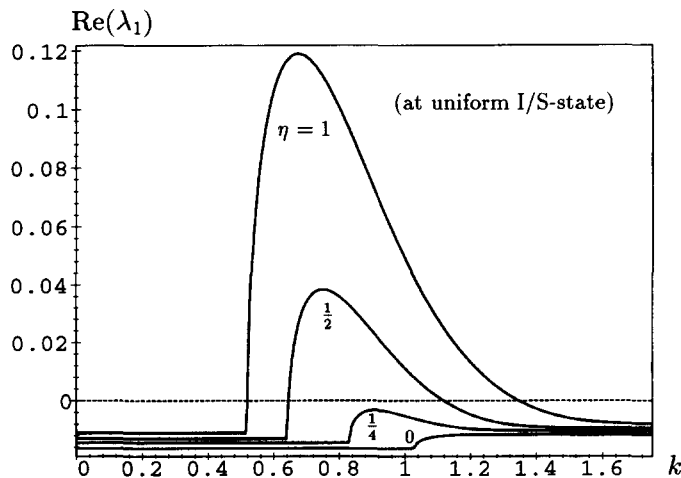


Fig. 4. Real part of the dominant eigenvalue  $\lambda_1$  of  $A$  versus the spatial frequency  $k$ , for perturbations around the uniform I/S-state. Note that the band of unstable  $k$ -values disappears for low values of  $\eta$ .

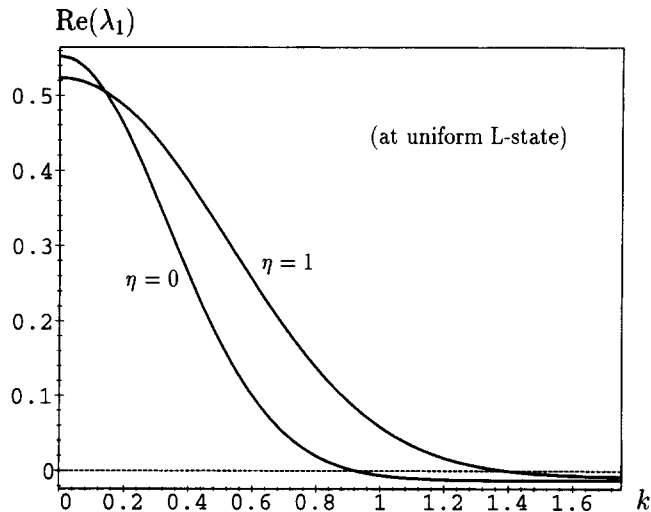


Fig. 5. Real part of the dominant eigenvalue  $\lambda_1$  of  $A$  versus the spatial frequency  $k$ , for perturbations around the uniform L-state. Only low- $k$  perturbations are unstable.

be a stable spiral node when constrained to remain a uniform state. This agrees with earlier results for a pair of discrete clones in both single-field [5] and two-field [6,7] models.

For all reasonably large  $\eta$ , however, the I/S-state is unstable to spatial modulations within a relatively narrow range of finite  $k$ . The wavelength for which  $\lambda_1$  is maximal should determine the distance between dot patterns which are formed when the solution starts at the uniform I/S-state or passes near to it during its transient. The width of the range of unstable  $k$  should be inversely related to the spatial scale over which the dot pattern is effectively periodic. These predictions are worked out and checked against simulations in the next section.

For low  $\eta$ , we find stability at any  $k$ . This clearly indicates a qualitative difference between the more realistic two-field model (say with  $\eta = 1$ ) and the previous single-field models (as emulated in the present model by taking  $\eta = 0$ ).

Figs. 5 and 6 show the same quantity  $\text{Re}(\lambda_1)$ , but now for perturbations around the L-state and the H-state, respectively. In both cases, the fastest growing modes are at  $k = 0$ . Thus, these fixed points are saddle points even when considering only uniform perturbations. The unstable and stable directions of these saddles differ between the two states: The diagonal ( $b_1 = b_2$ ) direction is the unstable one for the L-saddle, but the stable one for the H-saddle. The converse applies to the directions perpendicular to the diagonal at the L- and H-saddles.

The V-state is found to be stable for all  $k$  and  $\eta$ . The corresponding  $\lambda_1$ -plot is essentially featureless, so it is not shown. The stability is maintained for virtually any choice of the other parameters. This fits the fact that very small perturbations do not trigger an immune response.

### 3.3. Comparison with numerical simulations

The results of the spatial stability analysis should describe well the initial phases of the pattern formation, up to the point when the nonlinearity (hump shape) of the  $f(h_i, h'_i)$ -function starts to dominate the dynamics. Usually, the pattern predicted by the linear analysis determines the essential structure of the final nonlinear pattern, but in our case, there may be several instabilities which cause subsequent drastic changes in the pattern which arose first. Moreover, there may be essentially nonlinear processes which do affect the structure patterns. Comparing the results

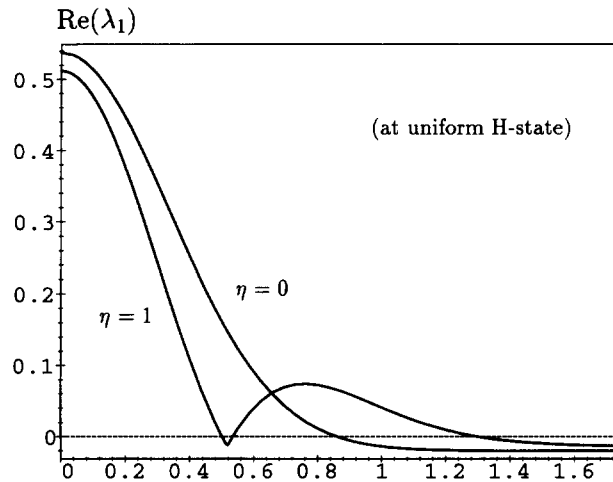


Fig. 6. Real part of the dominant eigenvalue  $\lambda_1$  of  $A$  versus the spatial frequency  $k$ , for perturbations around the uniform H-state. Realistically large  $\eta$  values cause a non-monotonic  $k$ -dependence.

of linear analysis against numerical simulations allows us to see to which extent the behaviour of the model can be captured analytically.

To investigate this, we have simulated the pattern formation starting from (or passing near to) each of the uniform fixed points, perturbed slightly by white spatial noise (which was also uncorrelated between  $i = 1, 2$  pairs). Figs. 7–11 (and Fig. 2 shown before) are numerically computed space–time plots of the (grey-coded) levels  $b_1(x)$  and  $b_2(x)$ , using a one-dimensional, circular space  $x$  to allow easy visualisation. Except for  $\eta$ , the same ‘standard’ parameters (see Table 1) were used in all figures shown. We compare the more realistic  $\eta = 1$  version to the one with  $\eta = 0$ , which corresponds to previous single-field models. We have also simulated the system for dimension  $n = 2$ , for other boundary conditions, and for other parameters, but these results are not shown since they support the same general conclusions. However, a different pattern formation scenario should occur for sufficiently large shape-space dimensions ( $n > 4$  for the standard parameters), where the uniform I/S-state and its inverse no longer exist (the L- and H-states disappear soon after), as noted above. Simulating this regime numerically is highly demanding, and we have only done some preliminary analysis to characterise the phenomena. We will come back to this issue in the concluding remarks.

### 3.3.1. Pattern formation near the uniform I/S-state

Fig. 7 shows the evolution of the system for  $\eta = 1$ , starting from the uniform I/S-state, with small random perturbations. The linearly unstable  $k$ -components (see Fig. 4) in the perturbation develop into a (nearly) periodic spatial pattern, with the modulations  $b_1(x)$  and  $b_2(x)$  being spatially in-phase, as determined by the corresponding eigenvector. The observed wavelength and the time scale for growth of the pattern correspond well with the analytical results (Fig. 4).

As the growing amplitude of the spatially modulated pattern reaches the strongly nonlinear regime, both  $b_i(x)$  levels saturate to a very small value (roughly the V-state) over a large part of the spatial cycle. However, the spatial wavelength remains the same ( $\pm 3\%$ ) as that of the linearly most unstable mode. The minor changes that do occur can be seen to involve the relaxation of occasional phase mismatches which exist in the early stages of the spatial modulation pattern. These transient violations of strict periodicity stem from the random nature of the perturbations,

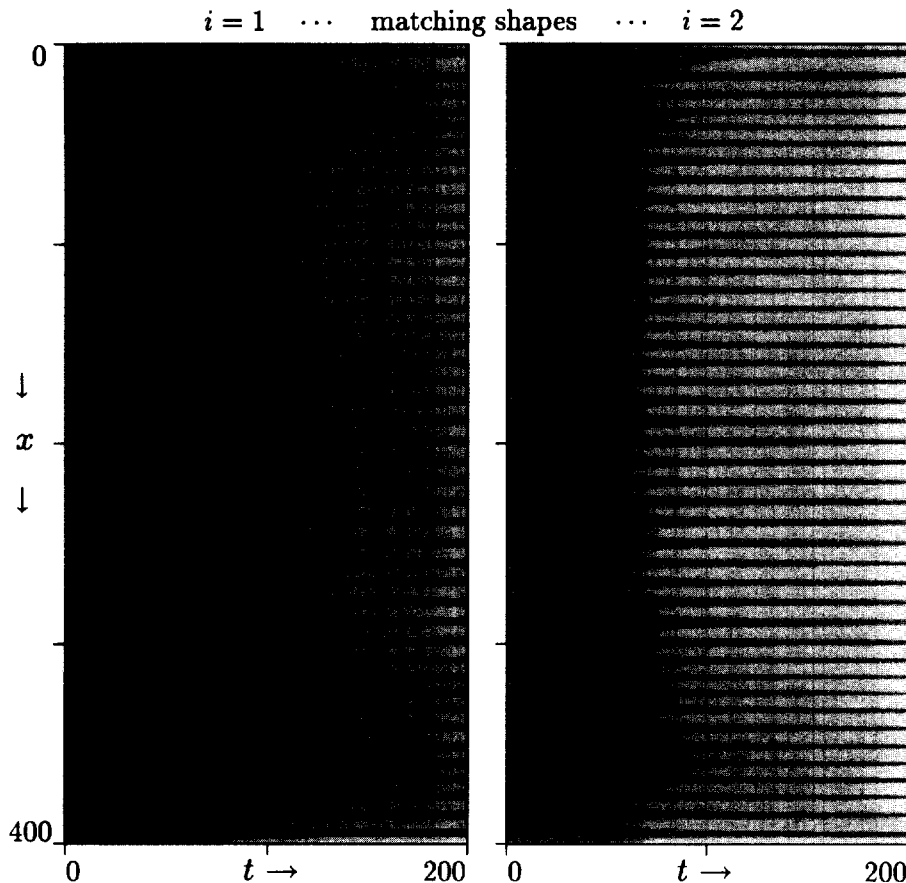


Fig. 7. Pattern formation starting from the (perturbed) uniform I/S-state, for  $\eta = 1$ . Grey-scale coded space–time plots of clone levels  $b_i(x)$  versus time  $t$ . The shape–space geometry is as in Fig. 2, and the model parameters are the ‘standard’ set. See text for interpretation of pattern formation processes.

combined with the finite width of the unstable  $k$ -range (see below for a quantitative discussion of the analogous effect on a low- $k$  unstable mode).

Ultimately, ‘dots’ of relatively small but finite width remain at the maxima of the periodic waveform. A dot consists of a pair of  $b_i(x)$  peaks at the same  $x$ . The individual levels are unequal, as determined essentially by the nonlinearities. In fact, the  $i = 1, 2$ -levels of a dot are qualitatively similar to those of the I/S-state of an isolated pair of discrete clones. Thus, we refer to ‘I/S-dots’, or to ‘S/I-dots’ when the roles of  $i$  and  $j$  are reversed. Note that a uniform I/S-state can only fragment into I/S-dots, and vice versa.<sup>2</sup>

Simulations for low  $\eta$  (not shown) confirm that such (essentially single-field) models have a uniform I/S-state which is stable to spatial perturbations of any  $k$ .

### 3.3.2. Pattern formation near the uniform H-state, and beyond

Fig. 8 shows the pattern formation for  $\eta = 1$ , starting from a randomly perturbed uniform state midway between the L- and H-states. This initial state flows quickly (in a few time units, just visible) along the diagonal to the H-state.

<sup>2</sup> Simulations in  $n > 1$  dimensions confirm that the final pattern consists of dots, rather than ‘stripes’ or ‘sheets’, even though such alternative patterns may occur as transient states near certain boundaries.

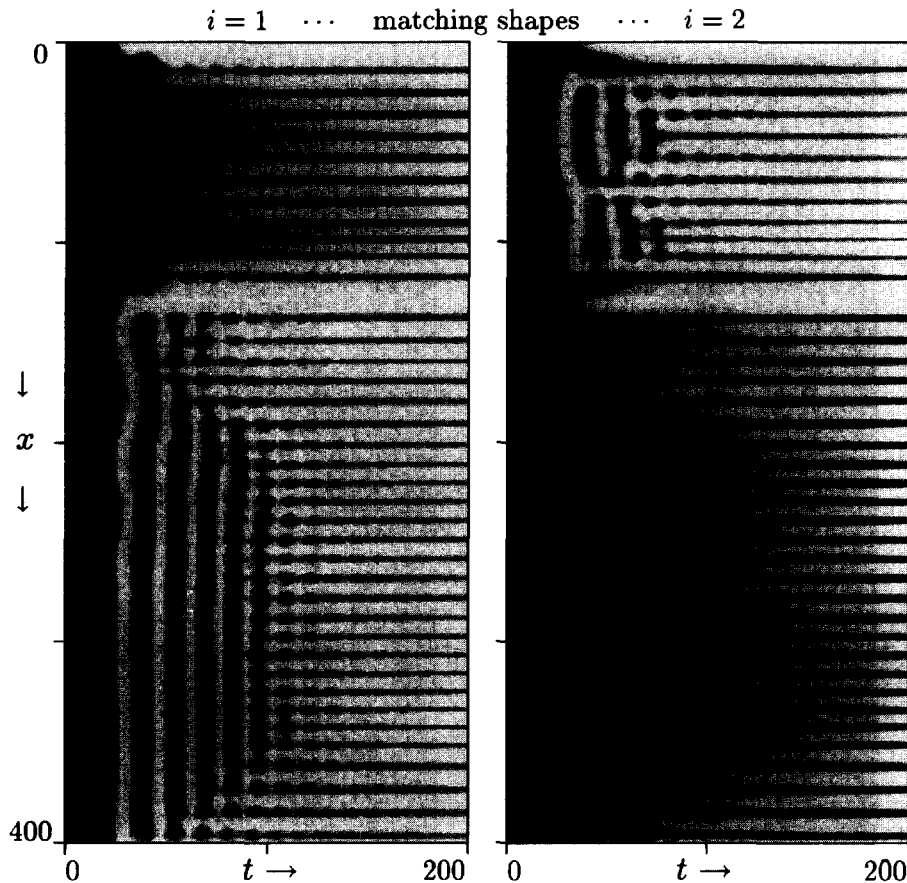


Fig. 8. Pattern formation from (randomly perturbed) uniform symmetric state between L and H, for  $\eta = 1$ . Grey-scale coded space–time plots of clone levels  $b_i(x)$  versus time  $t$ . Shape-space geometry and model parameters are as before. See text for interpretation.

Near the H-state, the trajectory slows down as expected. The pattern formation which occurs from then on can be seen to involve essentially two stages: First, the uniform H-state breaks up into large unequal-sized domains (with clone levels which undergo a damped oscillation). Next, all but the smallest of these domains break up further into quasi-regular arrays of dots.

The first stage, domain formation, illustrates our analytical finding that the H-state is a saddle point with respect to low- $k$  perturbations (see Fig. 6), and that the unstable directions of this saddle are perpendicular to the diagonal. The fact that the fastest growing mode occurs at  $k = 0$  does not imply that the solution should evolve *uniformly* along one of the unstable directions towards either the I/S- or the S/I-state under any practical conditions (even if one neglects the subsequent spatial instability of the latter states). In fact, linear analysis predicts the formation of coarse-scale but finite domains which approach either the I/S- or the S/I-state. Qualitatively, such domains develop because the random initial perturbations bias the local dynamics inhomogeneously towards the I/S- or the S/I-state, while the finite range of  $k$  with  $\text{Re}(\lambda_1) > 0$  allows a superposition of finite- $k$  noise components to grow. The typical size of the random domains may be estimated as follows.

As long as linearisation applies, the time-dependent spectral amplitudes of the perturbations, denoted by  $a(k, t)$ , grow essentially as  $a(k, t) = a(k, 0) \exp[\rho(k)t]$ , where  $\rho(k) = \text{Re}[\lambda_1(k)]$ , and sub-dominant eigenvalues are neglected. The  $a(k, t)$  are zero-mean Gaussian random variables with a variance we denote as  $V(k, t)$ . The initial

perturbations are uncorrelated (white), i.e.  $V(k, 0)$  is a constant. The typical domain-size we seek is given by the width of the spatial autocorrelation function, which we can compute in its spectral form, i.e. the normalised energy spectrum  $E(k, t) = V(k, t)/V(0, t)$ . Indeed, one has  $\ln[E(k, t)] = 2t(\rho(k) - \rho(0))$ . Since our estimate should be dominated by the behaviour near the maximum of  $E(k, t)$ , we retain only the leading term in the small- $k$  expansion, say  $tk^2/(2\tau)$ . Thus,  $E(k, t)$  is roughly a Gaussian of width  $\sqrt{\tau/t}$ , and this transforms to a Gaussian autocorrelation peak of width  $\sqrt{t/\tau}$ . This width estimates the characteristic spatial scale of the noisy  $b_i(x)$  modulations at time  $t$  into the transient. The  $\sqrt{t}$ -dependence reflects a very fast initial blurring of the white-noise perturbations, to a correlation scale which soon exceeds the scale  $\sigma$  of the field kernels. Equally, it predicts that the blurring decelerates quickly. Growth should essentially stop when the exponentially growing typical amplitude of the perturbations reaches the nonlinear regime. This characteristic time  $t^*$  depends only logarithmically on the typical amplitude of the initial random perturbations. At  $t \geq t^*$  (but before any subsequent instabilities), one should see rather well-defined domains, with random sizes up to  $\sqrt{t^*/\tau}$ .

In the second stage, the break-up of the I/S- and S/I-domains into dots depends on the finite- $k$  instability of these states that we have already analysed and simulated, but the scenario is not entirely the same. In the present case, the boundaries of the I/S-type domains form a locally much stronger perturbation of the I/S-state than the relevant

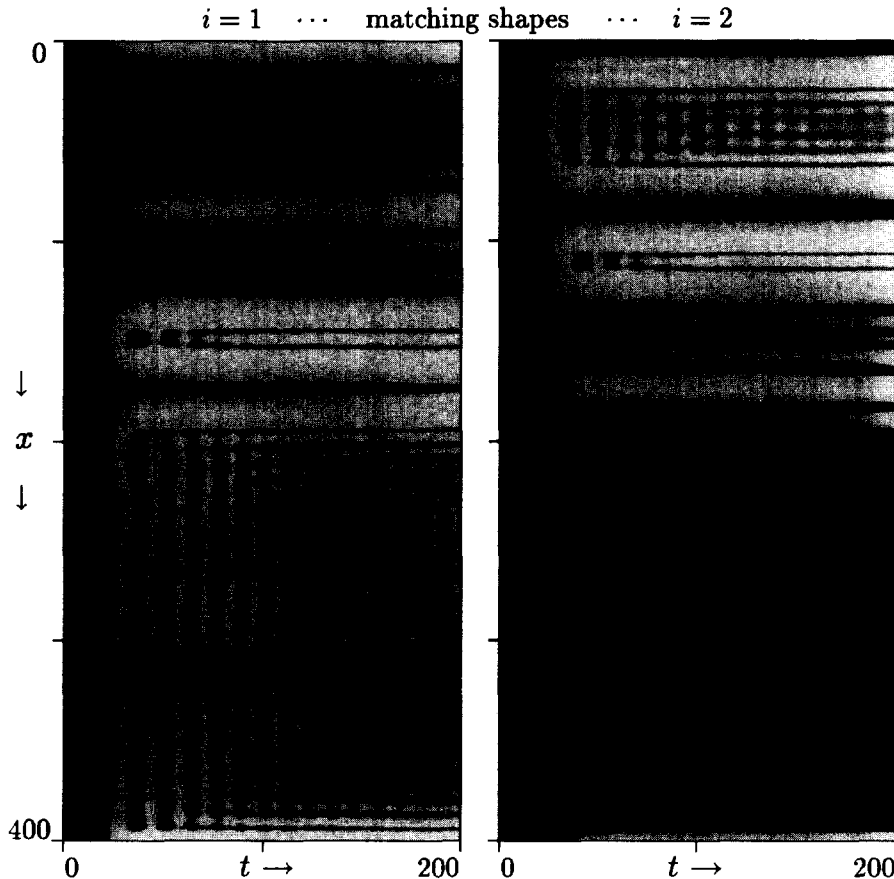


Fig. 9. Pattern formation from (randomly perturbed) uniform symmetric state between L and H, for  $\eta = 0$ . Grey-scale coded space-time plots of clone levels  $b_i(x)$  versus time  $t$ . Shape-space geometry and other parameters are as before. See text for interpretation.

perturbations in the centres of the domains, which have not grown very much by the time the domains arise. (Note that in the linearisation around the H-state, the  $k \approx 0.7$  band relevant to the second stage I/S-instability has much smaller eigenvalues than those near  $k = 0$ .) This explains why the array of dots appears initially as growing inward from the domain boundaries. In the centre of large enough domains, however, the break-up into dots must occur *before* the arrival of the inward propagation, since the exponential growth of local perturbations outcompetes any finite speed of a propagating front. This effect is clearly visible in the largest domain in Fig. 8.

The analogous simulation with  $\eta = 0$  yields Fig. 9. The initial stage still consists of the formation of random I/S- and S/I-domains, in accordance with the linear stability analysis and the domain-growth estimates given for the case  $\eta = 1$ . No subsequent fragmentation of the domains into dots occurs for  $\eta = 0$ , reflecting the linear stability of the uniform I/S-state in this case. The domain boundaries still act as strong perturbations, and we cannot rely on the linear analysis to determine their fate. The simulations do show pairs of strong (spatially offset) boundary overshoots which cause a striped perturbation further into the domains, but there is no trace of a nonlinearly propagating break-up process.

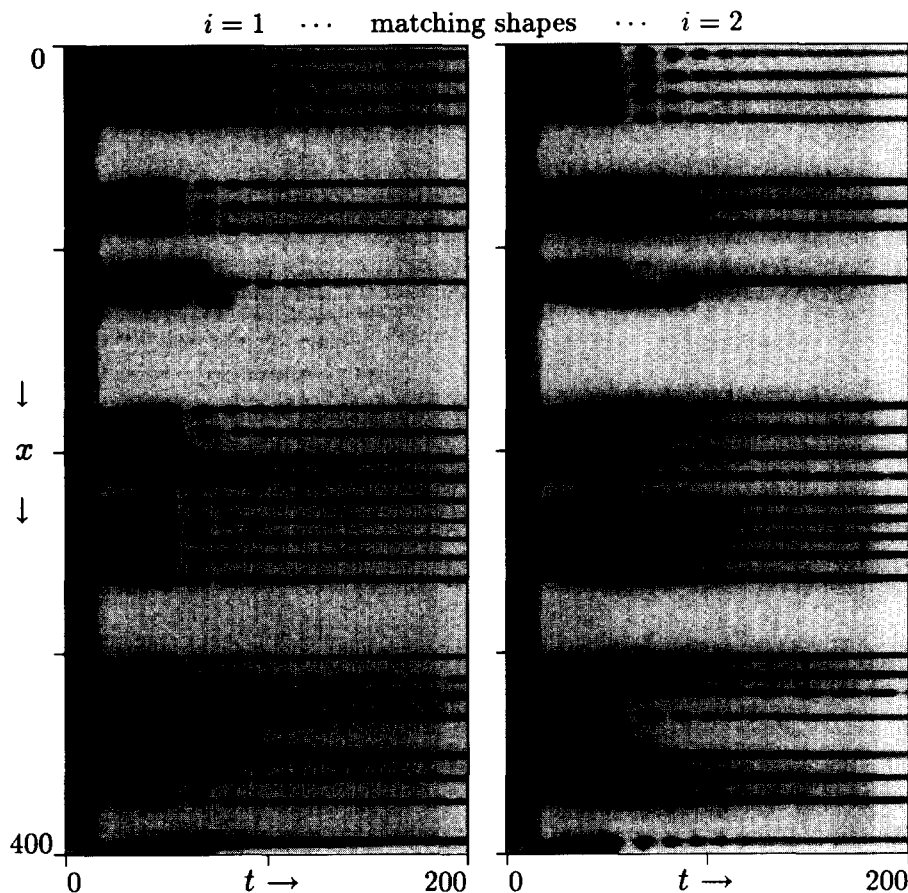


Fig. 10. Pattern formation from (randomly perturbed) uniform L-state, for  $\eta = 1$ . Grey-scale coded space-time plots of clone levels  $b_i(x)$  versus time  $t$ . Shape-space geometry and other parameters are as before. See text for interpretation.

### 3.3.3. Pattern formation near the uniform L-state, and beyond

Fig. 10 shows the pattern formation starting from a randomly perturbed uniform L-state, for  $\eta = 1$ . The motivating example shown early in this paper (Fig. 2) showed the same simulation, except for the use of another realisation of the random perturbations.

The most apparent new feature in the evolution from the L-state is the early emergence of V-state domains (white); the other domains initially go to the H-state. This early stage can be understood by recalling that the L-state is a saddle point with respect to low- $k$  perturbations (see Fig. 5), and that its unstable direction is the diagonal  $b_1 = b_2$ . Thus, the L-instability again leads to coarse random domains, but each domain now evolves towards either the V-state or the H-state. The V-state is linearly stable to perturbations of any  $k$ . Together with the fact that we perturbed randomly around the exact L-state here, this explains the observation that roughly 50% of shape-space is taken up by V-domains. The other domains evolve relatively slowly when their state approaches the H-state, as expected for trajectories near a saddle point.

The next stage in the process is ruled in essence by the H-state instability we have already analysed, but there are some quantitative differences due to the finite size and irregularity of the H-domains. The probability that an H-domain breaks up into I/S- and S/I-(sub-)domains is less in smaller H-domains, since the perturbation components which break the symmetry are essentially independent of those that seeded the H-domains. Moreover, the subsequent break-up of each sub-domain into dots of the same I/S-polarity should be accelerated by the perturbations on the edges of the H-domains. As a result, the two-stage break-up of H-domains almost merges into one stage, especially in the smaller domains. Another fact illustrated by the figure is that none of the temporary or final patterns can propagate into the V-state. This extends the already known linear stability of the V-state. We therefore need not illustrate the lack of pattern formation from this state by an additional figure.

A related observation is that isolated dots can exist in a V-domain. This situation can be analysed at least by approximations, but to do so falls outside the scope of the present paper (cf. Section 4). The same goes for the limit-cycle oscillation which may occur when an I/S-dot and a S/I-dot are close neighbours.

The same simulation with  $\eta = 0$  is shown in Fig. 11. Apart from the already familiar absence of well-defined I/S- and S/I-dots, there is another difference with the case  $\eta = 1$  above. The large, nonlinear perturbations at the boundaries between an initial V-state domain and, say, an I/S-domain now propagate complicated patterns into the V-domains. Eventually, this appears to destroy the V-domains, except for a relatively narrow border-strip between irregular I/S- and S/I-domains (with large overshoots near their boundaries). Previously, this propagating instability was called ‘percolation’ [4,5].

## 4. Conclusions and outlook

Our analysis and simulations have produced a reasonably clear picture of when and how B-clone activity in an idiotypic immune network gives rise to a variety of shape-space patterns. If such patterns are indeed formed in real immune systems, then one expects that the type of pattern and its (in)stability towards propagation could be functionally important, since the response to a new antigen would depend on whether its position in shape-space is near to an existing dot or domain of either the same or the opposite polarity. Likewise, it is to be expected that a localised, temporary antigen input could create a local dot of the polarity representing immunity against that antigen.

Note, however, that such dot-based effects only occur in a certain parameter regime. In fact, the  $\eta$  parameter of our two-field equations allows us to describe qualitatively distinct regimes, including the one in which we see the propagation instabilities characteristic of the earlier one-field type of B-cell network models.

We have characterised in detail the fundamentally different behaviour in the high- $\eta$  and low- $\eta$  regimes by linear stability analysis and numerical simulations. For realistically high values of  $\eta$ , the system either decays to the stable

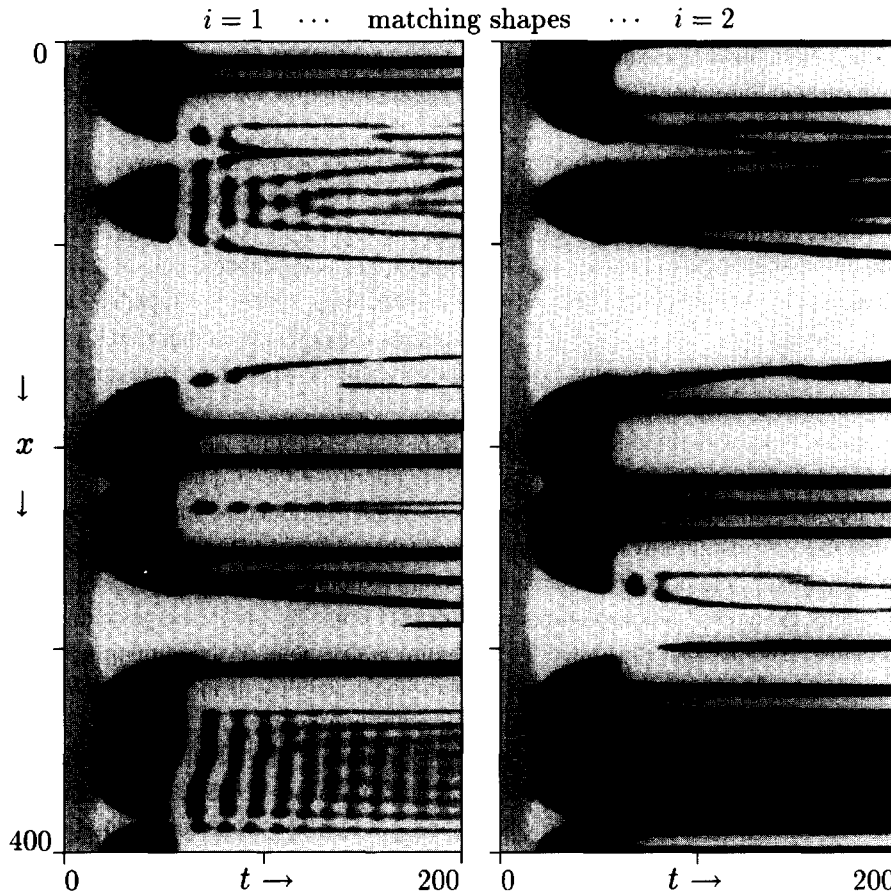


Fig. 11. Pattern formation from (randomly perturbed) uniform L-state, for  $\eta = 0$ . Grey-scale coded space–time plots of clone levels  $b_i(x)$  versus time  $t$ . Shape-space geometry and other parameters are as before. See text for interpretation.

V-state, or forms small, stable I/S- (or S/I-) dots, which can occur solitary or in arrays. For sufficiently low  $\eta$ , however, no such dots are formed, and the behaviour of our two-field model reverts to that of a classical single-field model, even though the equations assume the single-field form only at  $\eta = 0$ . The coarse domains with strong boundary overshoots which propagate unstable waves into the V-state for low  $\eta$  are similar to those seen previously in simulations of related single-field models [4]. The basic feature responsible for these differences is the behaviour of the activation function  $f(h, h')$  as illustrated in Fig. 1: For high  $\eta$ , clones at any  $b_i$  which are coupled by a too low  $K$  cannot stimulate each other sufficiently to cause net growth. For low  $\eta$ , however, the curves merely shift to the right, so that clones which are only coupled weakly, can still stimulate each other. As noted in [6], this property of the previous models leads to the propagation (percolation) of local perturbations throughout the network.

Our present model also differs from previous ones (with the exception of [7]) in the structure of the shape-space. In most earlier models, a point in shape-space represented a *single* shape, and matching pairs were found at pairs of positions related by a smooth mapping  $\mu$  (with  $\mu^2$  equal to the identity). For example, in [3,4], the map  $\mu$  was a reflection in a special point, which represents a self-complementary shape. Other reasonable mappings could introduce more complicated self-complementary loci. One important consequence of such a structure is that all uniform states must have  $b_i = b_j$ , in our notation. This excludes the existence of the uniform I/S-state which we have found to be an important precursor of dot patterns for realistic  $\eta$ . In addition, the stability analysis of the

remaining uniform fixed points (with  $b_1 = b_2$ ) then reflects not just the properties of the state per se, but also those that are peculiar to the self-matching at the special locus [10]. Disentangling these very distinct effects can be problematic.

Our homogeneous shape-space structure excludes any self-complementary points. This allows a simpler and more complete analysis, but it is by no means impossible that self-complementary shapes exist in reality. The analysis in the present paper is formally unable to say anything about the possible consequences of self-complementarity for pattern formation, but (for realistic  $\eta$ ) we expect only local effects near the special loci, because no substantial propagation of instabilities occurs; the dots are local, stable entities. At a distance of a few times  $\sigma$  from the special loci, our analysis should apply with very little change.

To capture pattern formation nearer to self-complementary loci, one needs an explicit model of the local shape-space geometry at such loci. There are many eligible geometries besides the central-inversion example mentioned. Explicit construction of such structures, and a study of their consequences for pattern formation lies beyond the scope of the present paper.

We noted the existence of a finite dimension ( $n = 4$  for standard parameters) above which the I/S- (and H- and L-) states cannot occur, leaving the V-state as the only uniform solution. However, this does not exclude the existence of stable (arrays of) dots. Numerical work in such high dimensions is very demanding, but preliminary results (using a coarse spatial grid) indicate that small I/S-dots indeed exist, and these appear to be the only stable pattern elements for high  $n$  and  $\eta = 1$ . In addition, we have confirmed analytically that I/S-dots of essentially one lattice-cell diameter (and certain arrays of these) are stable states in high- $n$  lattices. A more complete study of this regime is underway, but we can at least mention here a qualitative explanation for the fact that I/S-dots still exist for high  $n$ : The crucial feature is that the effective diameter of the dots becomes smaller than the scale  $\sigma$  of the binding field. As we noted earlier, the disappearance of the uniform I/S-state (and also L and H) for increasing  $n$  is due to the increasing ratio  $h_i/h'_i$  of the local binding and crosslinking fields. This lowers the maximum of the clone activation function  $f(h_i, h'_i)$  until no net growth is possible at all. Dots avoid this fate by being narrower than the binding-field kernel, which lowers  $h_i/h'_i$ .

We must also leave for another occasion the problem of analysing solitary dots within a V-state background. As stated earlier, this problem can be addressed at least at the level of various approximations. Given the existence of solitary dots, the translation invariance of the equations implies that even very weak noise should cause the dots to diffuse through space. This, in turn, leads to questions about the interactions between dots that approach each other closely. On the other hand, it is natural to break the strict spatial homogeneity, e.g. by adding a spatially random perturbation to the interaction parameter  $K$ . This should ‘pin down’ the dots at local maxima of  $K$ . Similar effects should be caused by the presence of self-antigens [7], or by the holes in the spatial distribution of the influx rate  $s$ , as created by selecting out self-reactive B-cells.

Finally, we may note that the dots formed in our model (with any reasonably large  $\eta$ ) are long-lived entities, which have the same polarity as the local excursion in the initial conditions which created the dot (or array of dots, for broad excursions). To the extent that our model captures the essential behaviour of B-cell clones in real immune systems, the existence of such dots should constitute a ‘memory’ for antigens, without any reliance on specialised memory cells.

## Acknowledgements

AJN thanks Pauline Hogeweg for apt and fruitful criticism of an early version of this work. AJN and KT thank SLW/NWO for financial support.

## Appendix A. Exact uniform fixed-point solutions

It is worth noting that the uniform clone levels  $b_i$  and their fields play essentially the same role as the corresponding quantities in a version of the basic model equations (1)–(4) with only two *discrete* clones; the original binding and crosslinking interactions  $K$  and  $K^{\eta+1}$  are rescaled to  $\kappa$  and  $\gamma\kappa$ , see Eq. (8). Thus, solution of our fixed-point equations for general  $\kappa$  and  $\gamma$  includes as a special case the discrete 2-clone problem which was explored earlier [6].

### A.1. Fixed-point equalities and approximations

For ease of reference, we write down again the quadratic equation obtained from the fixed point conditions  $\partial_t b_i = 0$  for general  $s$

$$-db_i^2 + [p\theta\phi(b_j) - d\theta + s]b_i + s\theta = 0. \quad (\text{A.1})$$

The  $s = 0$  case of this simplifies to

$$b_i = \theta \left( \frac{p}{d}\phi(b_j) - 1 \right), \quad (\text{A.2})$$

which clearly requires  $\phi(b_j) > d/p$  to yield meaningful solutions. Otherwise, the only  $s = 0$  solution is the trivial  $b_i = 0$ .

The relation of the  $s > 0$  result to the one for  $s = 0$  is made apparent by writing the roots of Eq. (A.1) as

$$b_i = \frac{1}{2} \left\{ b_i^* + \frac{s}{d} \pm \sqrt{\left( b_i^* + \frac{s}{d} \right)^2 + 4\frac{s\theta}{d}} \right\}, \quad (\text{A.3})$$

where  $b_i^*$  is shorthand for the non-trivial  $s = 0$  fixed-point expression, Eq. (A.2). Only the larger of the pair of roots (plus-sign in Eq. (A.3)) is biologically meaningful, except in the limiting case  $s = 0$  where the lower root (minus-sign) gives the trivial solution  $b_i = 0$ .

The equalities given so far suffice for constructing the solutions exactly, but some insight can be gained by approximating the relevant root of Eq. (A.3) in either of two ways, i.e. as

$$b_i \approx b_i^* + \frac{s}{d} + \frac{s\theta}{db_i^* + s}, \quad (\text{A.4})$$

which requires  $db_i^* + s \gg 2\sqrt{sd\theta}$ , or as

$$b_i \approx -\frac{s\theta}{db_i^* + s}, \quad (\text{A.5})$$

which requires the inverse condition  $db_i^* + s \ll -2\sqrt{sd\theta}$ . These regimes have a clear interpretation: In the first case, the clone is sustained essentially by its activation, while in the second case, it is sustained essentially by the small influx  $s$ . The narrow ‘crossover’ region (roughly  $|db_i^* + s| < 2\sqrt{sd\theta}$ ) between the two regimes vanishes as  $s \rightarrow 0$ .

In addition, it may be noted that the fixed-point equation of the  $\theta \rightarrow \infty$  limit (5) of the model becomes

$$b_i = \frac{s}{d - p\phi(b_j)}. \quad (\text{A.6})$$

The meaningful solutions now require  $\phi(b_j) < d/p$ , and  $s > 0$ . Given that typical  $s$ -values are 4–6 orders of magnitude smaller than the  $b$ -values at the fixed points, it is clear from Eq. (A.6) that the system would have to be

very close to the ‘blow-up’ point  $\phi(b_j) = d/p$ . One may show that this causes the fixed point to be almost neutrally stable (exactly so as  $s \rightarrow 0$ ). This unrealistic feature is absent for finite  $\theta$ , even if  $\theta$  is several times larger than the clone levels at fixed points.

### A.2. Constructing the exact fixed points for $s = 0$

The pair of equalities (A.2) can be solved for pairs  $b_1, b_2$  simply by substituting the  $b_1$ -equation into the right-hand side of the one for  $b_2$ , and simplifying the result. This yields a rational function in  $b_2$  (too large to print here) which is equated to zero. The numerator polynomial, denoted as  $P_5(b_2)$ , has degree 5, so there can be at most five fixed-point solutions, namely the roots of  $P_5$ . At this stage, it would appear that closed-form expressions for these solutions are unobtainable, as is the case for roots of generic fifth degree polynomials.

However, the  $(i, j)$ -permutation symmetry of the pair of equations (A.2) implies that its solutions  $(b_i, b_j)$  either are symmetric ( $b_i = b_j = b$ ), or else they come in pairs  $(b_1, b_2)$  and  $(b_2, b_1)$  with  $b_1 \neq b_2$ . Thus, if there are an odd number of distinct solutions (five at most), then an odd number of these must be symmetric. Finding such symmetric solutions simplifies finding the others, as follows.

To find the symmetric fixed points, one substitutes  $b_i = b_j = b$  into Eq. (A.2) and rearranges it into the rational function equality

$$\frac{w\kappa^2b^3 + (\theta w\kappa + 2w + \gamma)\kappa b^2 + \{\theta\kappa[2w + \gamma(1 - \delta)] + w\}b + \theta w}{w\kappa^2b^2 + (2w + \gamma)\kappa b + w} = 0, \quad (\text{A.7})$$

where  $\delta = p(1 + 4w)/d$ . Denoting the third degree numerator polynomial above by  $P_3(b)$ , one concludes that there are up to three symmetric fixed points, which must be real-valued roots of  $P_3(b)$ . Classical expressions [11] yield the roots of  $P_3(b)$ , and the conditions under which some or all of these are real and positive. These expressions are too large to print here, but they are easily handled by common computer-algebra packages.

To construct the non-symmetric fixed points, one may start by noting that all roots of  $P_3(b)$  are also roots of  $P_5(b)$ . Thus, any roots of  $P_5(b)$  that are *not* roots of  $P_3(b)$  must be roots of  $P_5(b)/P_3(b)$ , which is at most a quadratic polynomial, to be denoted as  $P_2(b)$ . Explicitly, one gets

$$\begin{aligned} P_2(b) = & [w(\kappa\theta - 1)^2 - \theta\gamma\kappa]w\kappa^2b^2 \\ & + \{w\theta^2\kappa^2[2w + \gamma(1 - \delta)] + \theta\kappa[\delta(2w + \gamma^2) - (2w + \gamma)^2] + w(2w\gamma)\}\kappa b \\ & + w^2(\theta\kappa - 1)^2 + (\delta - 1)w\theta\gamma\kappa. \end{aligned} \quad (\text{A.8})$$

Thus, one of the components (say  $b_j$ ) of the non-symmetric fixed points is obtained in closed form simply by writing down the roots of  $P_2(b_j) = 0$ , and checking whether they are real and non-negative. Expressing these conditions in terms of the parameters is of course straightforward, but the results are too lengthy to warrant being written down here. The other component  $b_i$  of each non-symmetric uniform fixed-point solution is then found by substituting the corresponding  $P_2$ -root  $b_j$  into Eq. (A.2).

Using computer-algebra, the resulting expressions can be used also to construct exactly the Jacobian at the fixed points, and from it the spectrum of eigenvalues which determine the (in)stability of small spatial perturbations around the uniform states.

### A.3. Procedure for general $s$

The general strategy for finding the uniform fixed points exactly for  $s > 0$  is analogous to the case  $s = 0$ , but some extra complications occur. Hand calculation is now impractical almost from the start, but the solutions are

still easily obtainable by computer algebra. We need only sketch the points at which the procedure differs from the  $s = 0$  case.

To find the symmetric solutions, one substitutes  $b_i = b_j = b$  into Eq. (A.1), and simplifies. This results in a rational function with a fourth degree numerator polynomial, the real-valued positive roots of which are the solutions we seek. Classical expressions [11] yield closed (but very large) forms for the roots and the conditions under which they are positive.

Finding the non-symmetric solutions is less straightforward than previously, because a direct substitution of the quadratic  $b_i$ -roots (Eq. (A.3)) into Eq. (A.1), with  $i$  and  $j$  interchanged, would introduce irrationals. However, one may still solve the system purely within the field of polynomial equations, by standard algorithms based on the Grobner formalism, as implemented in virtually any computer-algebra system (e.g. Mathematica or Maple). The result is another fourth degree polynomial (much larger than the former) for the non-symmetric  $b_i$  fixed points. Its roots are thus known in closed (but unwieldy) form, and the corresponding  $b_j$ -components of the solutions follow by substitution of the  $b_i$ -roots into Eq. (A.3), taking the larger root.

The fact that these higher-degree equations still have no more than two non-symmetric and three symmetric solutions (under our restrictions on the signs of parameters and solutions) is not readily perceived in the exact results. In this respect, the simple and intuitive construction sketched in the main text is to be preferred.

## References

- [1] I.M. Roitt, *Essential Immunology* (Blackwell, Oxford, 1994).
- [2] N.K. Jerne, Toward a network theory of the immune system, *Ann. Immunol* 125 C (1974) 373–389.
- [3] L.A. Segel and A.S. Perelson, Computations in shape-space: A new approach to immune network theory, in: *Theoretical Immunology II, SFI Studies in the Science of Complexity, Vol. III* (Addison-Wesley, Redwood City, CA, 1988) pp. 321–343.
- [4] R.J. de Boer, L.A. Segel and A.S. Perelson, Pattern-formation in one- and two-dimensional shape-space models of the immune system, *J. Theoret. Biol.* 155 (1992) 295–333.
- [5] R.J. de Boer and P. Hogeweg, Unreasonable implications of reasonable idiotypic network assumptions, *Bull. Math. Biol.* 51 (1989) 381–408.
- [6] R.J. de Boer, M.C. Boerlijst, B. Sulzer and A.S. Perelson, A new bell-shaped function for idiotypic interactions based upon crosslinking, *Bull. Math. Biol.* 58 (1996) 285–312.
- [7] K Takumi and R.J. de Boer, Self assertion: Modelling a network repertoire of multi-determinant antibodies, *J. Theoret. Biol.* (1996), in press.
- [8] B. Sulzer, R.J. de Boer and A.S. Perelson, Crosslinking reconsidered: Binding and crosslinking fields and the cellular response, *Biophys. J.* 70 (1995) 1154–1168.
- [9] A.S. Perelson and G.F. Oster, Theoretical studies on clonal selection: Minimal antibody repertoire size and reliability of self-nonself discrimination, *J. Theoret. Biol.* 81 (1979) 64–670.
- [10] L.A. Segel and A.S. Perelson, A paradoxical instability caused by relatively short-range inhibition, *SIAM J. Appl. Math.* 50 (1990) 91–107.
- [11] M.A. Abramowitz and I.A. Stegun, *Handbook of Mathematical Functions*, 9th printing (Dover, New York, 1972).